The Astrophysical Journal, 966:27 (15pp), 2024 May 1 https://doi.org/10.3847/1538-4357/ad2eaa


# Solar Eruptions in Nested Magnetic Flux Systems

Judith T. Karpen[1], Pankaj Kumar[1,2], Peter F. Wyper[3], C. Richard DeVore[1], and Spiro K. Antiochos[4]
[1] Heliophysics Science Division, NASA Goddard Space Flight Center, Greenbelt, MD 20771, USA; judy.karpen@nasa.gov
[2] Department of Physics, American University, Washington, DC 20016, USA
[3] Department of Mathematical Sciences, Durham University, Durham, DH1 3LE, UK
[4] CLaSP, University of Michigan, Ann Arbor, MI 48109, USA
*Received 2024 January 4; revised 2024 February 21; accepted 2024 February 22; published 2024 April 23*

## Abstract

The magnetic topology of erupting regions on the Sun is a key factor in the energy buildup and release, and the subsequent evolution of flares and coronal mass ejections (CMEs). The presence/absence of null points and separatrices dictates whether and where current sheets form and magnetic reconnection occurs. Numerical simulations show that energy buildup and release via reconnection in the simplest configuration with a null, the embedded bipole, is a universal mechanism for solar eruptions. Here we demonstrate that a magnetic topology with nested bipoles and two nulls can account for more complex dynamics, such as failed eruptions and CME–jet interactions. We investigate the stalled eruption of a nested configuration on 2013 July 13 in NOAA Active Region 11791, in which a small bipole is embedded within a large transequatorial pseudo-streamer containing a null. In the studied event, the inner active region erupted, ejecting a small flux rope behind a shock accompanied by a flare; the flux rope then reconnected with pseudo-streamer flux and, rather than escaping intact, mainly distorted the pseudo-streamer null into a current sheet. EUV and coronagraph images revealed a weak shock and a faint collimated outflow from the pseudo-streamer. We analyzed Solar Dynamics Observatory and Solar TErrestrial RElations Observatory observations and compared the inferred magnetic evolution and dynamics with three-dimensional magnetohydrodynamics simulations of a simplified representation of this nested fan-spine system. The results suggest that the difference between breakout reconnection at the inner null and at the outer null naturally accounts for the observed weak jet and stalled ejection. We discuss the general implications of our results for failed eruptions.

*Unified Astronomy Thesaurus concepts:* Solar coronal mass ejections (310); Solar activity (1475); Solar magnetic reconnection (1504); Solar magnetic fields (1503)

*Supporting material:* animations

## 1. Introduction

The wide variety of eruptive phenomena observed on the Sun poses enduring mysteries. Why do some filament channels erupt fully, driving mass and magnetic flux into the heliosphere, while others produce no ejecta or ejecta that do not escape the corona (e.g., Svestka & Cliver 1992; Kumar et al. 2011; Shen et al. 2012; Cui et al. 2018; DeRosa & Barnes 2018; Mason et al. 2021; Kumar et al. 2022; Li et al. 2022; Duan et al. 2023; Kazachenko 2023)? This is an important question with societal relevance because destructive space weather is largely caused by solar eruptions, resulting in spacecraft failures and premature deorbiting, communications blackouts, and human impacts ranging from radiation damage to power-grid shutdowns. To understand the physical mechanisms behind these eruptions and ultimately predict them, we must understand the full spectrum of eruptive behavior. Toward that aim, it is equally important to comprehend what prevents, as well as what enables, eruptions.

The availability of high-resolution EUV imaging from more than one viewpoint has enabled significant insight into this problem, aided by photospheric magnetograms and extrapolations of the coronal magnetic fields in the erupting regions. Greater understanding is gained by combining such observations with numerical simulations of systems that incorporate the important characteristics and allow the governing parameters to be varied. Here we describe, in detail, observations of an eruption that began as a fast filament ejection, but then stalled and produced only a weak coronal jet. In this paper, we focus on presenting the observations and their analysis, but include a data-inspired simulation that captures accurately the topology of the system and allows us to give a physical interpretation for the observed dynamics.

The leading models for eruption initiation invoke ideal or resistive mechanisms, each of which requires an imbalance in physical forces. In every model, outward-directed forces (e.g., magnetic pressure) must prevail over inward-directed forces (e.g., magnetic tension) to obtain an eruption. This imbalance must apply not only locally during initiation but throughout the subsequent rise through the corona to allow the erupting flux to escape. In the simplest example of the magnetic breakout model (Antiochos 1998; Antiochos et al. 1999; MacNeice et al. 2004; Karpen et al. 2012), consisting of a bipole embedded in a global dipolar field (also known as a fan-spine topology), the basic eruption process is well understood, and has been shown to account for both coronal mass ejections (CMEs) and coronal jets depending on the parameters of the system (Wyper et al. 2017). Energy is built up through accumulated magnetic shear in the closed field beneath the separatrix surface, increasing the internal magnetic pressure and causing the overlying coronal null to

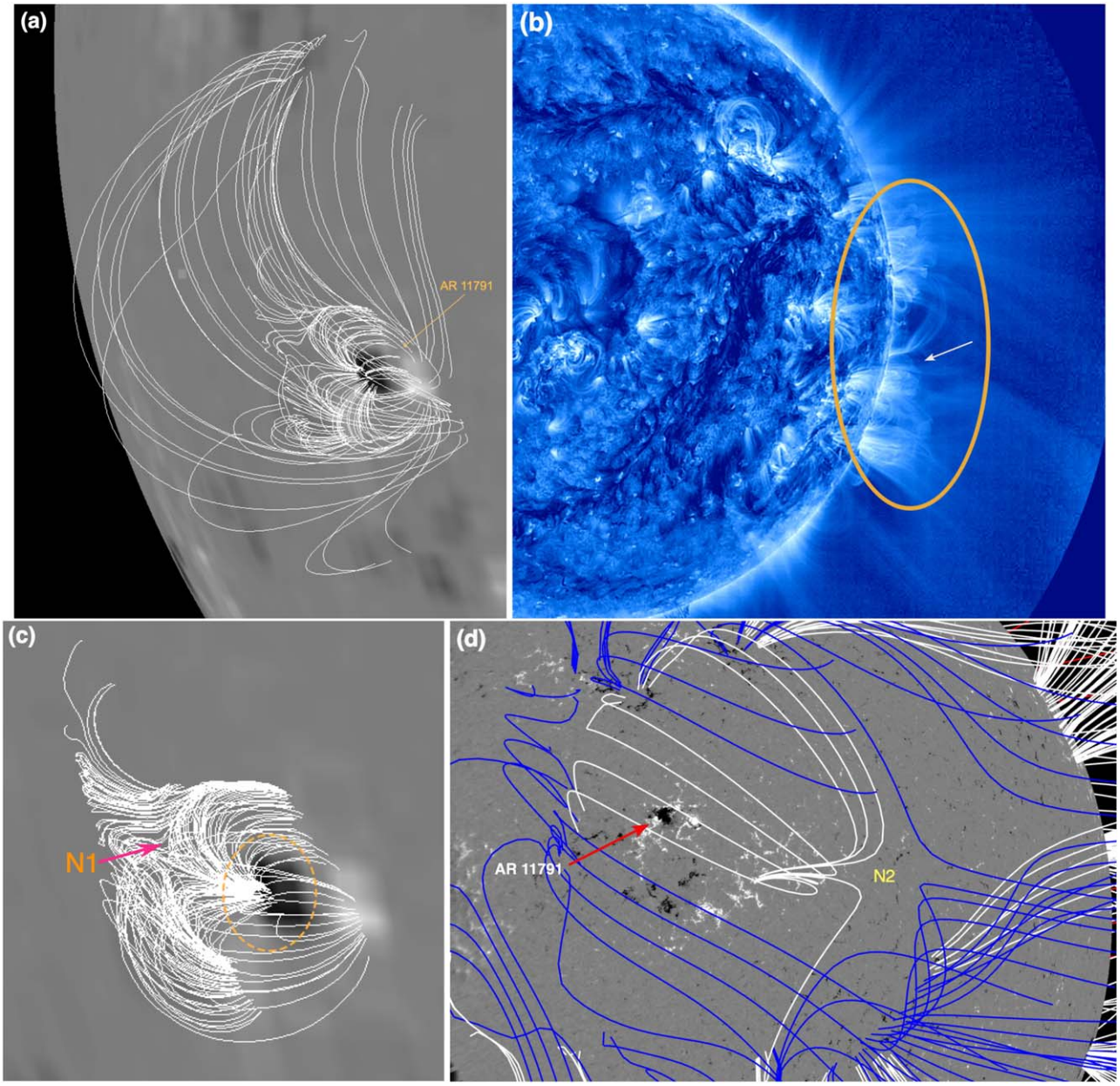


**Figure 1.** (a) PFSS extrapolation of AR 11791 (marked by an arrow) using an SDO/HMI magnetogram (B scaled between ±200 G) at 00:04:00 UT on 2013 July 13. (b) STEREO-B EUVI 171 Å image at 04:14:00 UT. The orange oval encompasses the pseudo-streamer base. The arrow indicates the approximate location of the AR (partially behind the limb). (c) Zoomed-in view of the PFSS extrapolation of AR 11791, highlighting its fan-spine topology. The approximate location of its coronal null (N1) is marked. The orange dashed oval indicates the approximate location of the PIL. (d) PFSS extrapolation of the entire pseudo-streamer (zoomed-out view) magnetic field along with a rotated view toward the disk center. The northern portion of the pseudo-streamer enclosing AR 11791 is shown in panel (a). The selected field lines in panels (a) and (c) are overlaid on the lower-resolution synoptic maps, whereas the field lines in (d) are overlaid on a full-resolution HMI magnetogram (0.″5 per pixel). Blue field lines are open, white field lines are closed. The approximate location of the pseudo-streamer coronal null (N2) is marked.

distort into a current sheet. Reconnection through this so-called breakout sheet removes overlying magnetic flux, reducing the tension force that holds down the expanding stressed flux. For fast eruption to occur, a second current sheet must form beneath the rising flux and lengthen until a critical length-to-width aspect ratio is reached. Reconnection onset in this so-called flare current sheet (FCS) creates a flux rope above and an arcade of flare loops below, and accelerates the breakout reconnection in a feedback process. Ideal instabilities such as kinking could enable or assist in this scenario, after the flux rope is formed and the appropriate instability criterion is met. In any case, the eruption requirements are (i) sufficient energy buildup to initiate breakout reconnection, (ii) creation of a FCS that meets the criteria for reconnection onset, and (iii) sufficient breakout reconnection to remove a critical amount of the constraining flux. In the solar environment, these apparently simple requirements depend on a multitude of conditions from the photosphere to the corona: the surrounding field strength and morphology, the energy buildup process or processes, the presence and number of topological features such as nulls and separators, and the physics of reconnection under solar

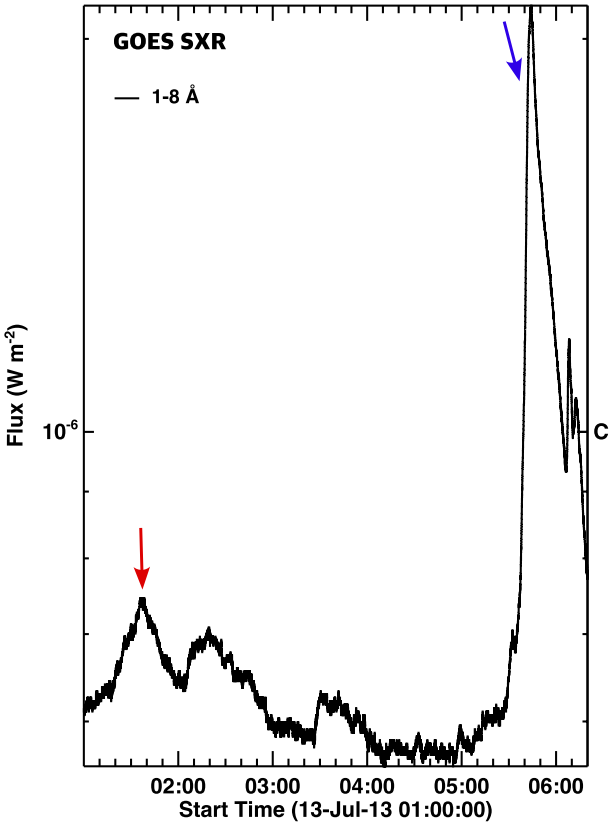


**Figure 2.** GOES soft X-ray flux profile showing the confined B7.4 flare (red arrow) and the main C1.4 eruptive flare (blue arrow).

conditions. Other eruption models have an equally daunting list of competing and enabling factors in the initiation phase. However, once a flux rope is formed, they all face the same set of gateways and obstacles determining whether eruption occurs.

The event described in this paper comes from a combination of two simple topologies: a small fan-spine configuration associated with a small active region (AR) nested inside a large fan-spine configuration associated with a large pseudo-streamer (Wang et al. 2007). This configuration offers two opportunities for breakout reconnection, at the inner and outer nulls. Such a "double-breakout" situation may seem especially conducive to producing an explosive eruption, but in fact is likely to lead to a failed eruption, as we show below. In this event, the inner system ejected a flux rope that drove a shock ahead of it, but the flux rope stalled at the outer fan separatrix, producing a faint, jet-like mass flow that reached only a few solar radii. By analyzing this uncommon though not unique event, we confirmed that the inner eruption followed the breakout paradigm, and we identified features during its subsequent evolution that indicate strong interactions between the erupting flux system and the outer fan-spine field. Motivated by the observations, we performed a numerical simulation parameter study of eruption in a nested magnetic topology. In this paper, we compare the observations with a numerical simulation that closely reproduced the observed behavior, to derive an intuitive physical understanding of eruptions in nested magnetic systems. The full computational parameter study is reserved for a separate paper (P. F. Wyper et al. 2024, in preparation).

## 2. Data

We analyzed Solar Dynamics Observatory (SDO)/Atmospheric Imaging Assembly (AIA; Lemen et al. 2012) full-disk images of the Sun (field of view $\approx 1.3\,R_{\odot}$) with a spatial resolution of $1\farcs5$ ($0\farcs6$ pixel$^{-1}$) and a cadence of 12 s, in the following channels: 171 Å (Fe IX; $T \approx 0.7$ MK), 193 Å (Fe XII, Fe XXIV; $T \approx 1.2$ MK and $\approx 20$ MK), and 211 Å (Fe XIV; $T \approx 2$ MK), 131 Å (Fe VIII, Fe XXI, Fe XXIII; i.e., $T \approx 0.4$, 10, 16 MK) images. The three-dimensional noise-gating technique (DeForest 2017) was used to clean the images. This well-established technique highlights statistically significant features in image sequences down to the instrumental resolution, while attenuating the background noise through a choice of algorithms and filters. To determine the underlying magnetic topology of the investigated region, we utilized potential-field source surface (PFSS) extrapolations. The extrapolations shown in Figure 1(a) and (c) were produced by the PFSS package available in SSWIDL IDL, while the extrapolation in (d) was produced by the PFSS package built into Jhelioviewer (see Müller et al. 2017 for details). Both packages use as input the synoptic magnetograms, which have a resolution of $256 \times 180$ in a sine-latitude grid.

The Extreme Ultraviolet Imager (EUVI; Wuelser et al. 2004; Howard et al. 2008) on Solar TErrestrial RElations Observatory Behind (STEREO-B) observed the same event close to the west limb. On 2013 July 13, the separation angle between SDO and STEREO-B was $-138.7°$, while the separation angle between the Solar and Heliospheric Observatory (SOHO)/Large Angle and Spectrometric Coronagraph (LASCO) and STEREO-B was $-138.6°$. We used EUVI-B 195 Å images (10 min cadence) to view the morphology of the AR from this different viewing angle. The size of the STEREO/EUVI image is $2048 \times 2048$ pixels ($1\farcs6$ pixel$^{-1}$), covering a field of view out to $1.7\,R_{\odot}$. We utilized STEREO-B COR1 (1.3–4 $R_{\odot}$; Thompson et al. 2003) and LASCO C2 (2–6 $R_{\odot}$; Brueckner et al. 1995) coronagraph images to view the CME signatures associated with the eruption.

To investigate the particle-acceleration sites during the C1.4-class flare associated with the filament eruption around 05:40 UT, we used hard X-ray light curves and images from the Reuven Ramaty High Energy Solar Spectroscopic Imager (RHESSI; Lin et al. 2002), reconstructed with the PIXON algorithm (Metcalf et al. 1996; Aschwanden et al. 2004). We adopted an integration time of 20 s for the image reconstruction in the 6–12 keV and 12–25 keV energy channels. We used dynamic radio spectra obtained by the Radio Solar Telescope Network Learmonth Radio Observatory from the low corona and Wind/WAVES (Bougeret et al. 1995) from the interplanetary medium.

## 3. Observations

### 3.1. Magnetic Configuration

The GOES C1.4-class flare occurred on 2013 July 13, 05:36–05:53 UT, in NOAA AR 11791, which was embedded within a large pseudo-streamer positioned between two coronal holes. The filament began to rise slowly around 05:18 UT, leading to an explosive eruption at 05:40 UT. Figure 1(a) shows a magnetogram several hours before the event from the SDO Helioseismic and Magnetic Imager (SDO/HMI), with the AR footpoints marked. A PFSS extrapolation from a

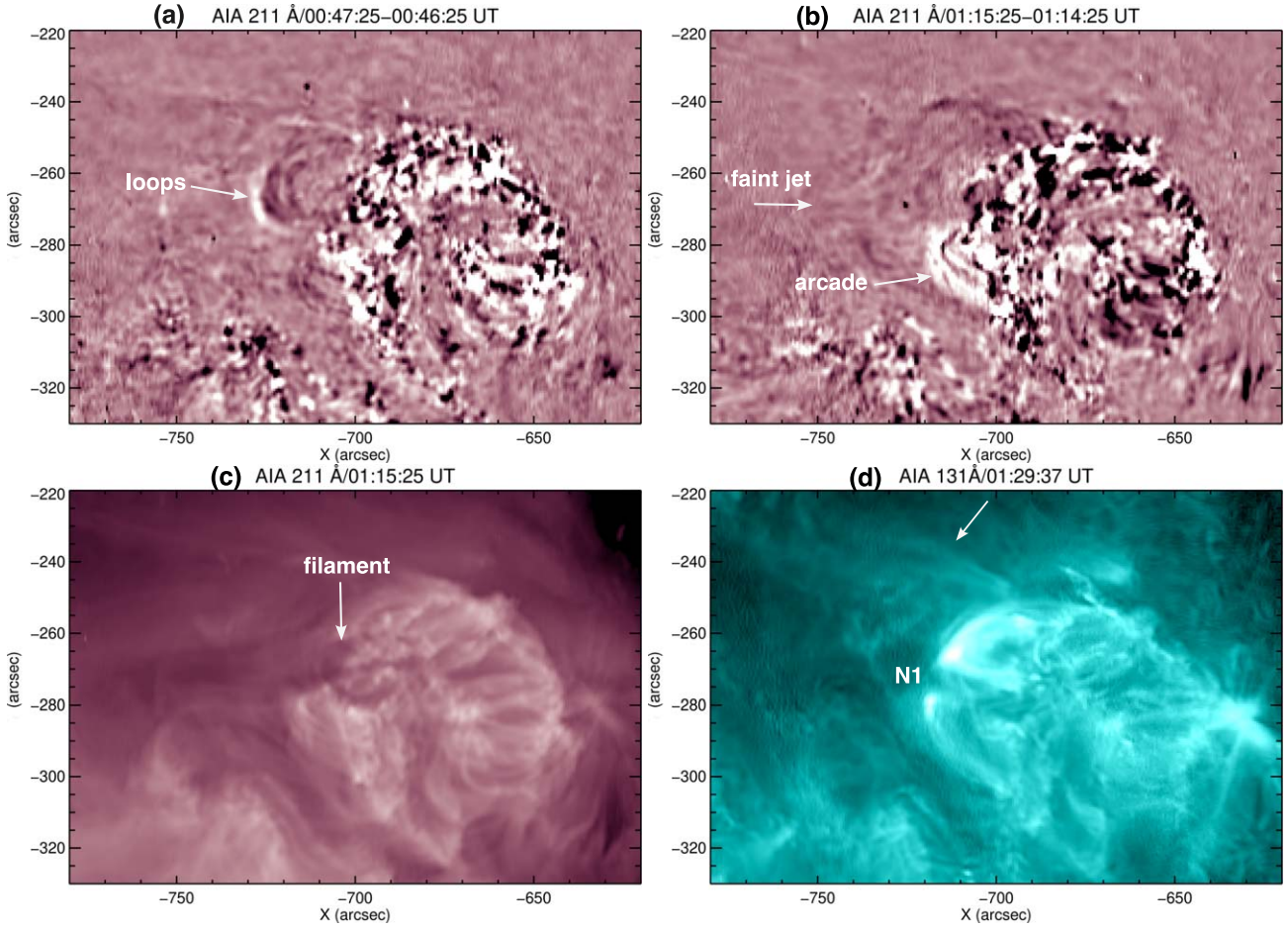


**Figure 3.** ((a), (b)) AIA 211 Å running-difference images at two times of the B7.4 flare, which produced expanding loops and faint jets above the PIL on the east side of the AR. Some flux was transferred from north to south. (c) AIA 211 Å image of the flaring region at the time of panel (b). The arrow marks the nonerupting dark filament. (d) AIA 131 Å snapshot of hot loops late in the B-class flare. The outer edge of brightened field lines opened by reconnection at null N1 is marked by an arrow. An animation of the AIA 211 and AIA 211 Å running-difference images is available online. The animation runs from 00:32:49 UT to 01:57:37 UT, and the duration is 8 s.

(An animation of this figure is available.)

magnetogram at 00:04:00 UT highlights the common basic topology of the two magnetic systems: fan-spine configurations characteristic of embedded bipoles (Antiochos 1998), each surmounted by a magnetic null point (Figure 1). The fan loops beneath the separatrix exhibit the characteristic "anemone" shape first noted by Shibata et al. (1994) in coronal-jet sources. Because of the difference in scale between the AR and the pseudo-streamer, Figure 1(c) zooms in to pinpoint the inner (AR) null, N1, while (d) zooms out to focus on the outer (pseudo-streamer) null, N2. Note that the system is asymmetric: the inner null is positioned on the east (left) side of the AR, while the outer null is offset substantially westward from the AR. The distribution of majority-polarity flux around the AR minority polarity was clearly uneven, with an apparent gap in the region where the minority flux extended eastward.

### 3.2. Pre-eruption Activity

AR 11791 began to activate around 01:00 UT and resumed a relatively quiescent state around 04:00 UT. The GOES-15 soft X-ray monitors detected a B7.4-class flare from AR 11791 that peaked around 01:38 UT, followed ≈4 hr later by a C1.4-class flare that accompanied the AR eruption (Figure 2). As shown in Figure 3(c), a filament occupied the northeastern and southeastern sections of the polarity inversion line (PIL), whereas dark fibrils traversed the western half of the PIL. The B-class flare was confined, consisting of brightenings in the inner fan loops, minor expansion of the northern portion of the fan, and faint jets above the AR PIL on the east side (Figure 3(a)–(c)). Although this was a minor flare, it produced significant emission and dynamics in AIA hot channels such as 94 and 131 Å. Some extended bright loops just outside the flaring region shifted northward, while transient flows propagated in both directions along the bright fan (Figure 3(d) and accompanying animation). The filament along the eastern side of the PIL remained unperturbed throughout this phase.

Figure 4 illustrates the dynamic evolution of the AR from the B-class flare through the C1.4 flare, in cotemporal AIA 304 Å images and HMI magnetograms. Focusing on the inter-flare period for now, we detected repeated episodes of fan-loop brightening, particularly in the northern fan, accompanied by vigorous flows along the loops. Adjacent arch filaments crossed the northern segment of the PIL at

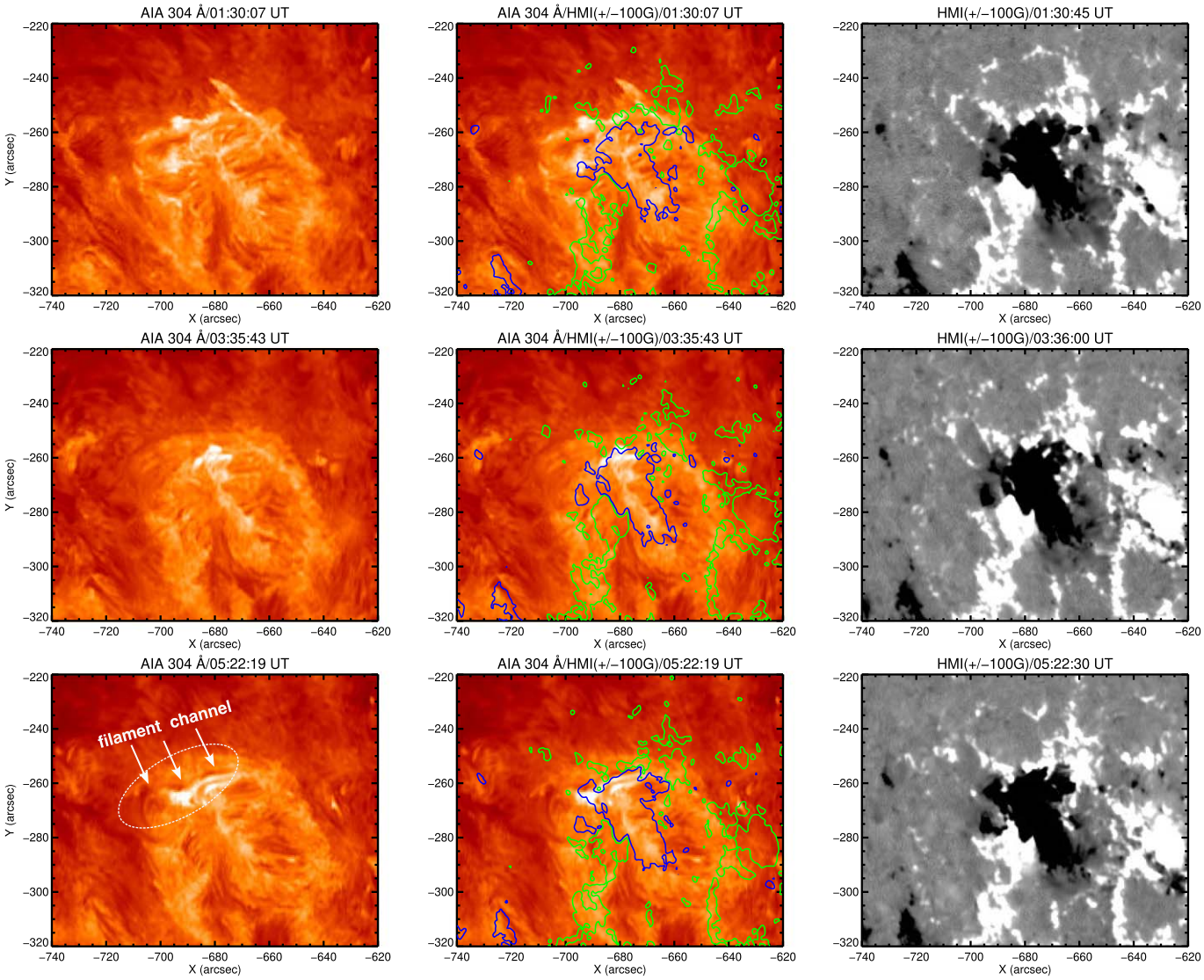


**Figure 4.** Activity during and after the B7.4 flare, prior to the C1.4 flare. Each row contains an AIA 304 Å image, the same image with superposed HMI contours at ±100 G, and the simultaneous HMI magnetogram. The first two times (top and middle) were selected to illustrate activity at the first and third small peaks in the GOES light curve (Figure 2). The last time (bottom row) depicts the precursor phase of the C1.4 flare. The filament channel is marked by arrows inside the dotted ellipse. An animation is available online. The animation runs from 00:36:45 UT to 06:51:00 UT, and the duration is 16 s.

(An animation of this figure is available.)

slightly different angles but remained nearly perpendicular to the PIL, in contrast to the filament aligned with the eastern PIL. Minor changes in the photospheric line-of-sight magnetic field occurred during this interval, but no major signs of emergence or cancellation were observed. The times of the three sets of images were chosen to align with the GOES-15 soft X-ray flux peaks. Early in this interval, the brightest 304 Å emission was located north and south of the filament; later, the brightest emission was located near the northern end of the filament. A bright remote ribbon repeatedly appeared and disappeared along the southeast boundary of the fan. Gradually the filament became obscured by luminous overlying loops. Type III bursts occurred at 03:10 UT and just before 04:00 UT, but in the absence of radio imaging it is unclear whether these electron-beam signatures were associated with the B-class flare or other solar activity.

### 3.3. Breakout and Impulsive Phase

Figures 5 and 6 and the accompanying animations show the evolution of the EUV-emitting plasma in the AR through the impulsive phase of the C1.4 flare. The first signs of activity associated with the main event appeared around 05:00 UT. Transient dynamic brightenings appeared throughout the anemone-shaped AR loop system, more concentrated in the northern half (underneath the filament). The emission intensity around the null fluctuated, then became substantially brighter around 05:10 UT while assuming a triangular shape. This region became sufficiently bright to produce the typical AIA diffraction pattern around 05:13 UT. A curved bright arc extended northwestward from the triangle in this phase, with the rising dark filament silhouetted against it from 05:18 UT until eruption. Faint loops above the filament rose slowly and protruded toward the east, becoming more distinct between

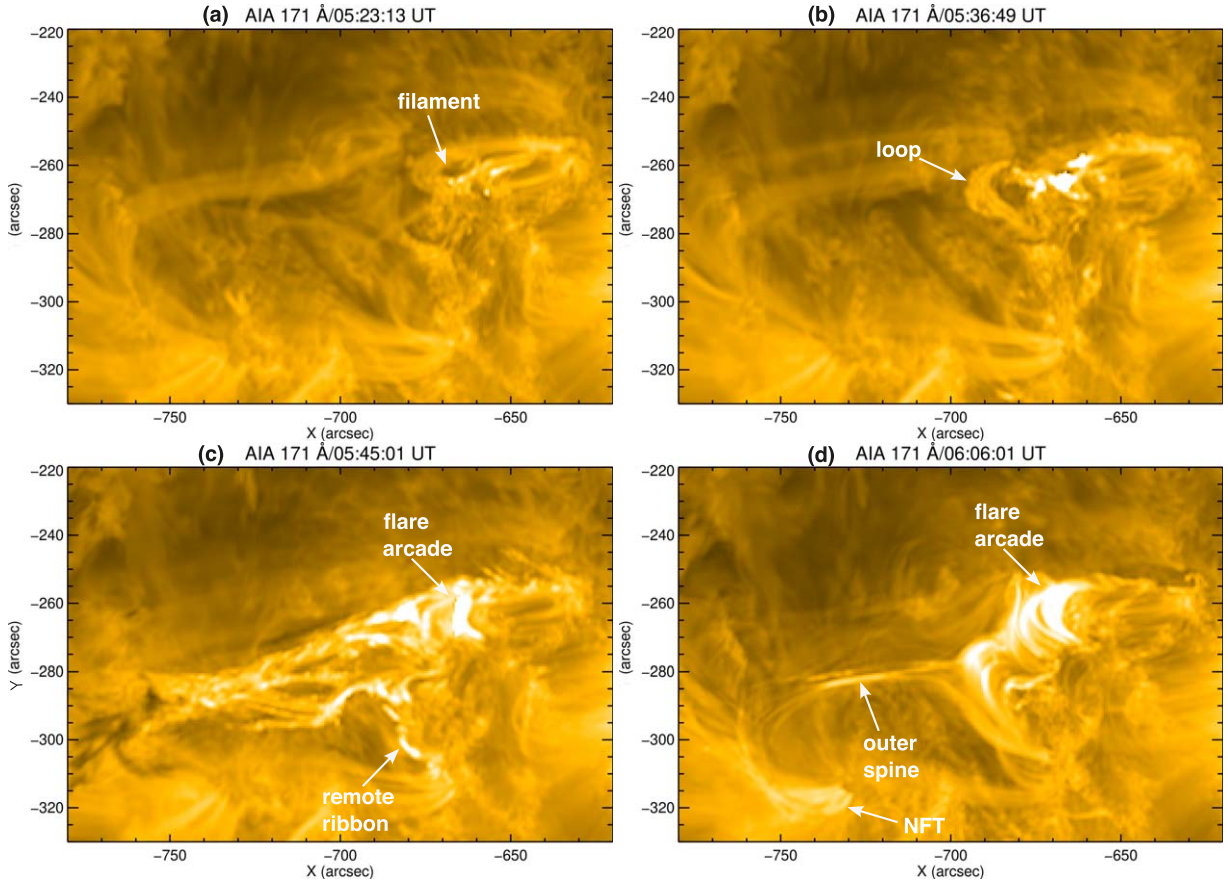


**Figure 5.** AIA 171 Å images at four times during the impulsive phase. Key features are labeled. (a) Slow rise of the filament (marked by an arrow) before the onset of the C1.4 flare. (b) A bright loop encloses the filament, which has risen significantly. The flare arcade west of the loop begins to brighten. (c) The flare arcade has expanded as the erupting filament extends beyond the frame. (d) The north leg of the erupting plasma has moved from inside to outside the frame. An arrow indicates the flows along the outer spine. An animation is available online. The animation runs from 05:01:37 UT to 06:57:25 UT, and the duration is 14 s. The animation has two parts. The left side shows a larger region, with a smaller area outlined in red. The right side shows this smaller region.

(An animation of this figure is available.)

05:25 and 05:30 UT. As shown in Figure 5(b), by 05:37 UT the filament had risen significantly, with a bright loop appearing ahead of it and a flare arcade brightening at the northern footpoint of that loop. By 05:45 UT, the erupting filament entwined in warm plasma extended far to the east, and a short remote ribbon was visible south of the flare arcade (Figure 5(c)). A striking change in the plasma configuration occurred shortly before 06:00 UT, when the north leg of the erupting filament apparently disappeared (Figure 5(d)). We explain this intriguing rearrangement in Section 5. Throughout this phase, multiple blobs (marked by an arrow at 05:37:49 UT in Figure 6(a)) and flows originated in or near the triangular feature and propagated northward. The size of the blobs is about 2″–3″. Shortly after the appearance of blobs ahead of the rising structure, we observed a narrow remote brightening (a third ribbon) indicated by an arrow at 05:40:13 UT in Figure 6(b), which traced footpoints of the side arcade (Figure 6(c)) observed in hot channels. These dynamic features are best seen in the animations accompanying Figures 5 and 6.

RHESSI observed the impulsive phase of the C1.4 flare in energy bands at 3–6 keV, 6–12 keV, and 12–25 keV (Figure 7). The highest-energy band peaked first, around 05:41 UT, closely followed by the two lower-energy bands at 05:42:30 UT. Figure 6 illustrates the relative locations of the X-ray and EUV emissions; RHESSI 6–12 (red) and 12–25 (blue) keV contours (at 20, 30, 50, 70, and 90% of peak intensity) are overlaid on the AIA 131 Å images. A single bright looptop source above the flare arcade appeared at 05:35 UT. A second source appeared during 05:42–05:45 UT, which coincided with the looptop source observed in EUV emission during the appearance of the side arcade associated with the remote ribbon (Figure 6 and accompanying animation).

### 3.4. Encounter with the Pseudo-streamer

The observations above—the intense C1.4 flare, the hard X-ray emission, and the fast rise of the flux rope—suggest that the eruption was indeed strongly explosive. The evolution changed dramatically, however, soon after the impulsive phase. The erupting plasma appeared to twist as it rose rapidly (headed eastward, from the AIA point of view), but it did not progress past a certain point. The ejection stalled. Threads of filament material were intertwined with the coronal-temperature plasma initially, then fragmented and fell from ∼06:00 UT onward after the flux rope reached its maximum extent. From the STEREO/EUVI point of view, the top of the erupting prominence flattened out at around 06:05 UT, and the north leg became disconnected from the surface around 06:06 UT

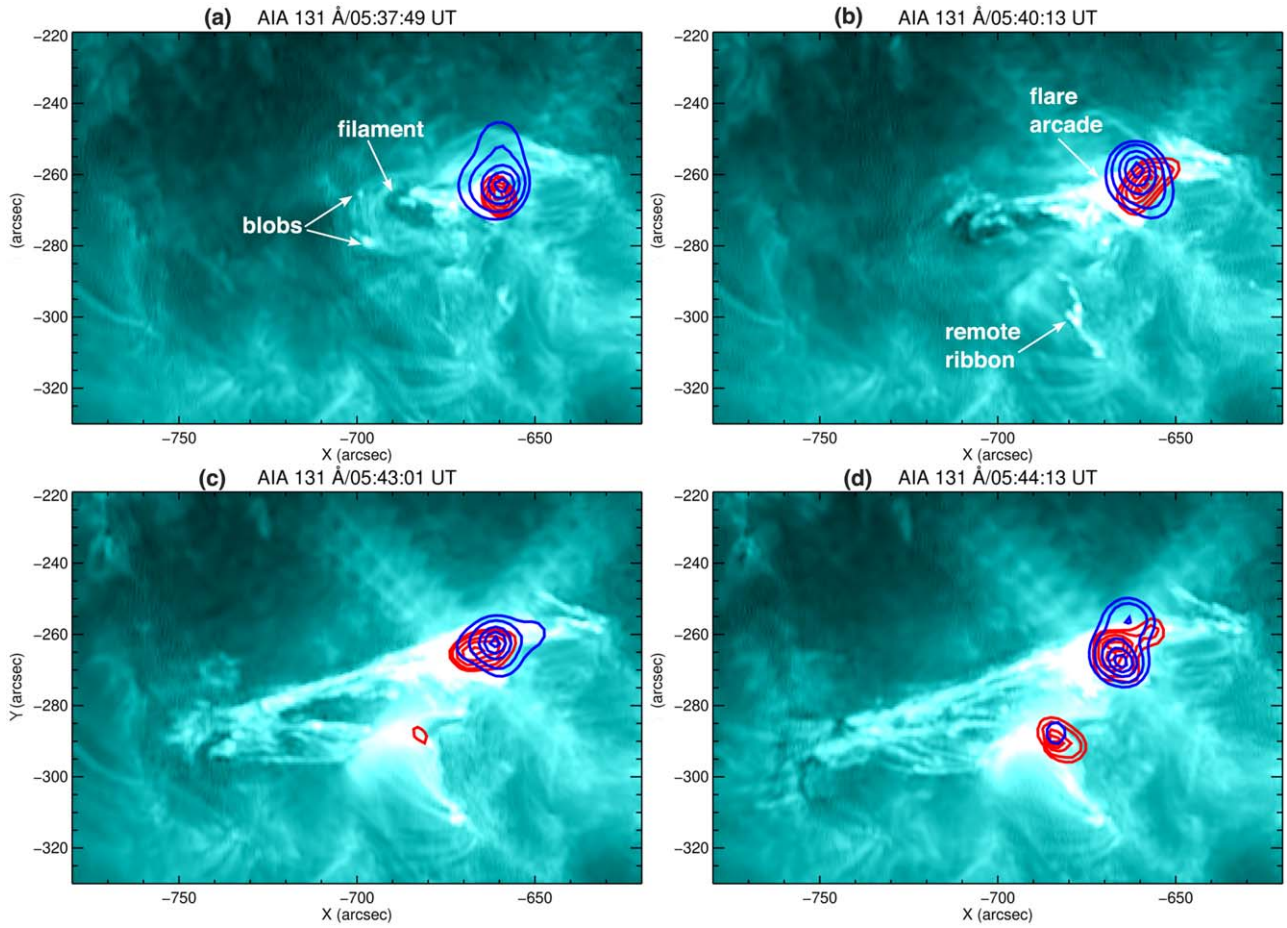


**Figure 6.** RHESSI 6–12 keV (red) and 12–25 keV (blue) contours overlaid on cotemporal AIA 131 Å images of the erupting region at four selected times during the impulsive phase of the C1.4 flare. Key features are labeled. (a) Bright blobs appear and propagate along the bright loops ahead (eastward) of the rising dark filament. A single looptop X-ray source is visible above the flare arcade. (b) The intensities of the looptop X-ray source and the hot flare arcade have increased. A narrow remote ribbon appears south of the flare ribbons. ((c), (d)) The eruption extends eastward. A secondary, more compact X-ray source appears and strengthens above the new side arcade, southeast of the initial X-ray looptop source and over the remote ribbon. An animation is available online. The animation runs from 05:35:01 UT to 05:44:37 UT, and the duration is 2.5 s.

(An animation of this figure is available.)

(Figure 8). From the AIA point of view, the north leg of the erupting plasma disconnected around 05:50 UT (Figure 5(d)), then the remnant became rooted in a new footpoint (marked NFT) south and east of the initial location after 05:45 UT (Figure 5(d) and accompanying animation). This striking connectivity change was not detected in our earlier studies of eruptions in single fan-spine topologies with overlying arcades, in either observations or simulations, which suggests that it is likely due to interactions between the erupting flux and the overlying pseudo-streamer field.

### 3.5. Outer Coronal Activity

The AIA imager and STEREO-B/COR1 and SOHO/LASCO coronagraphs registered faint but distinct activity associated with the C1.4 flare. The AIA 193 Å animation (Figure 9) clearly shows an EUV wave transiting the east limb just ahead of a slanting linear feature, followed by erupting plasma that stalled and fell back to the surface. Three features are visible in COR1: a broad oblique front first visible at 06:00 UT, propagating southward; a thin linear spike closer to the equator (Figure 10(a)); and a second front observable from 07:10 to 07:40 UT. In C2, the broad front propagated southward before fading out after 08:00 UT, but the second front is barely visible (Figure 10(b)). LASCO/C3 detected nothing, suggesting that the disturbances disappeared within a few solar radii.

Wind/WAVES (0.02–16 MHz) detected a Type III radio burst that coincided with the impulsive phase of the C1.4 flare at 05:42 UT. Narrow fainter Type IIIs were detected by the Learmonth radio observatory at metric frequencies, i.e., 25–180 MHz (Figure 11). These coronal and interplanetary Type IIIs are cotemporal with the hard X-ray emission observed by RHESSI.

## 4. Simulation

We used the three-dimensional Adaptively Refined Magnetohydrodynamics Solver (ARMS; DeVore & Antiochos 2008) to model a nested system with two null points whose fan-spine scales and photospheric magnetic flux densities are comparable to those of the observed system. ARMS has been employed extensively over many years to simulate breakout eruptions from null-point topologies on the Sun that produce flux-rope

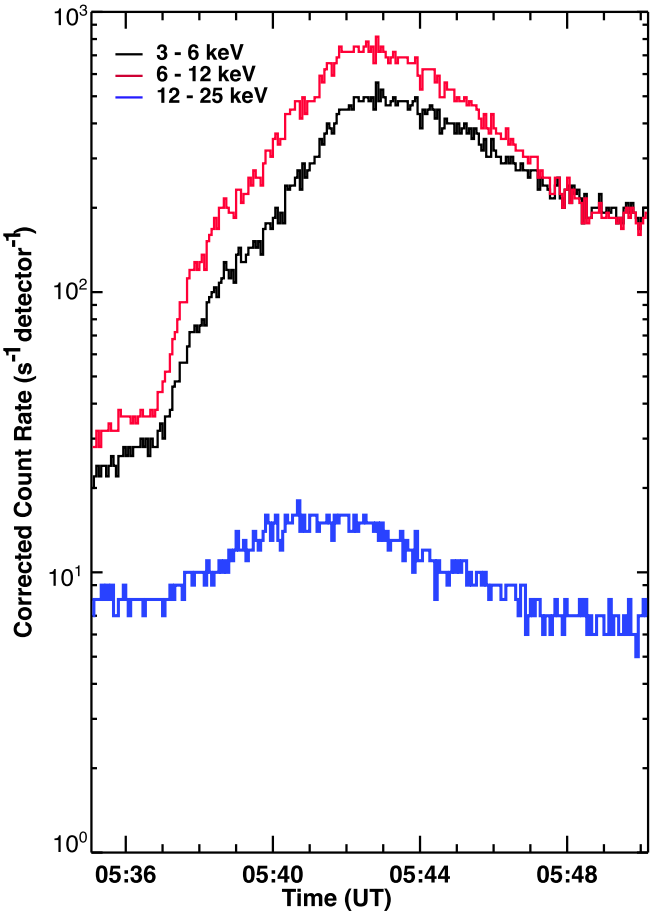


**Figure 7.** RHESSI light curves before and during the impulsive phase of the C1.4-class flare.

CMEs (Lynch et al. 2008; Masson et al. 2013; Lynch et al. 2016; Dahlin et al. 2019; Lynch et al. 2019; Masson et al. 2019; Lynch et al. 2021; Wyper et al. 2021) and collimated coronal jets (Pariat et al. 2009, 2010, 2015, 2016; Wyper & DeVore 2016; Wyper et al. 2016; Karpen et al. 2017; Wyper et al. 2017, 2018a, 2018b, 2019, 2022). Below, we summarize the essential features of the nested fan-spine simulation that best emulates the observed event described in the previous section. Further technical details of the calculation and the results of closely related simulations from our parametric study will be reported separately (P. F. Wyper et al. 2024, in preparation).

The computational domain is a spherical wedge with its outer radial boundary at $r = 10\ R_\odot$ and its side boundaries at $(\theta,\ \phi) = (\pm 63^\circ,\ \pm 113^\circ)$. The initial background plasma is an isothermal wind with temperature $T = 1$ MK and radial flow speed $v_r = 180$ km s$^{-1}$ at the outer boundary. The maximum grid refinement has a spatial resolution of $\approx$1.2 Mm at the equator. The initial magnetic configuration is shown in Figure 12(a). The pseudo-streamer is rooted in two elongated regions of negative flux positioned asymmetrically around an inner elongated region of positive polarity. Within the right lobe of the pseudo-streamer lies a strong embedded bipole of opposite orientation at much smaller size. The maximum photospheric flux density in the inner bipole is $\approx \pm 35$ G, while the pseudo-streamer field peaks at $\approx \pm 16$ G. The initial null heights are 0.08 $R_\odot$ and 0.49 $R_\odot$ for N1 and N2, respectively. The plasma $\beta$ is low throughout, between $\beta \approx 0.06$ at the base of the inner bipole and $\beta \approx 0.10$ at the base of the outer spine of the pseudo-streamer.

To energize the inner fan-spine system, surface flows were imposed in a narrow region around the inner PIL (Figure 12(b)). The flows were concentrated at the right side of the PIL to form a filament channel there. We assumed a subsonic, sub-Alfvénic peak flow speed of 25 km s$^{-1}$ to energize the magnetic field quasi-statically at reasonable computational cost. The footpoint driving was ramped up over 500 s, held constant for 9000 s, and ramped down over 500 s; this built up sufficient free energy to power an eruption. Figure 13 shows snapshots of midplane cuts through the evolving three-dimensional system from 9500 to 13,500 s during the calculation. Field lines and current density are shown in the top row, field lines and mass density in the bottom row. Starting at left, the panels depict the expansion of the energized magnetic flux inside the inner fan, forming a breakout current sheet (BCS) marked by an arrow; the initiation of a shock above the erupting flux rope formed by reconnection in the FCS; the escape of the shock and flux rope from the inner system and their interactions with the outer null and fan; and the release of a weak outflow from the pseudo-streamer, well behind the obliquely propagating shock. The inner system is relaxing toward its final state at the last time shown. This state is structurally similar to the original potential field, but with shear/twist distributed within flux tubes of both the pseudo-streamer and the embedded bipole.

The structural changes behind this activity sequence become clearer through inspection of the evolving magnetic configuration (Figure 14). In this series of simulation snapshots, line-tied flux-rope field lines rooted in the pseudo-streamer positive polarity are yellow, field lines initially rooted in the rightmost pseudo-streamer negative polarity are red, and inner fan-spine field lines rooted in either the pseudo-streamer positive polarity or the embedded-bipole positive polarity are green. As the filament-carrying flux rope (10,500 s) rises within the pseudo-streamer, it first reconnects through the inner null N1 with overlying flux, forging new connections between the inner and outer fans (11,500 s). In this way, a substantial amount of twist is transferred from the flux rope in the compact embedded-bipole system to the much larger pseudo-streamer flux system (12,500 s). The additional magnetic pressure within the pseudo-streamer distorts the outer null N2 into a second BCS, which enables reconnection between the closed pseudo-streamer flux and the external open flux. Some of the twist on the pseudo-streamer field lines is thereby transferred to newly reconnected field lines outside the pseudo-streamer null. The relaxation of this transferred twist drives a weak jet along the pseudo-streamer spine (Figure 15). The jet is denser than the surrounding plasma and has a peak speed $v \approx 300$ km s$^{-1}$, between the ambient sound and Alfvén speeds. The shock launched by the inner flux-rope eruption propagates at $v \approx$ 500 km s$^{-1}$, close to the ambient Alfvén/magnetosonic speed, and transforms into a progressively lower-amplitude wave. Most of the twist remains confined within the pseudo-streamer fan, and the system thereafter relaxes to a new equilibrium.

The dramatic changes in field-line connectivity that result from the eruption through the inner null point cause the footpoints of the twisted coronal flux rope to fragment and substantially reposition. The footpoints of the filament-carrying flux rope initially reside within the inner fan surface (10,500 s). When the flux rope reconnects through the inner null, its twist flux establishes new connections to footpoints outside the inner

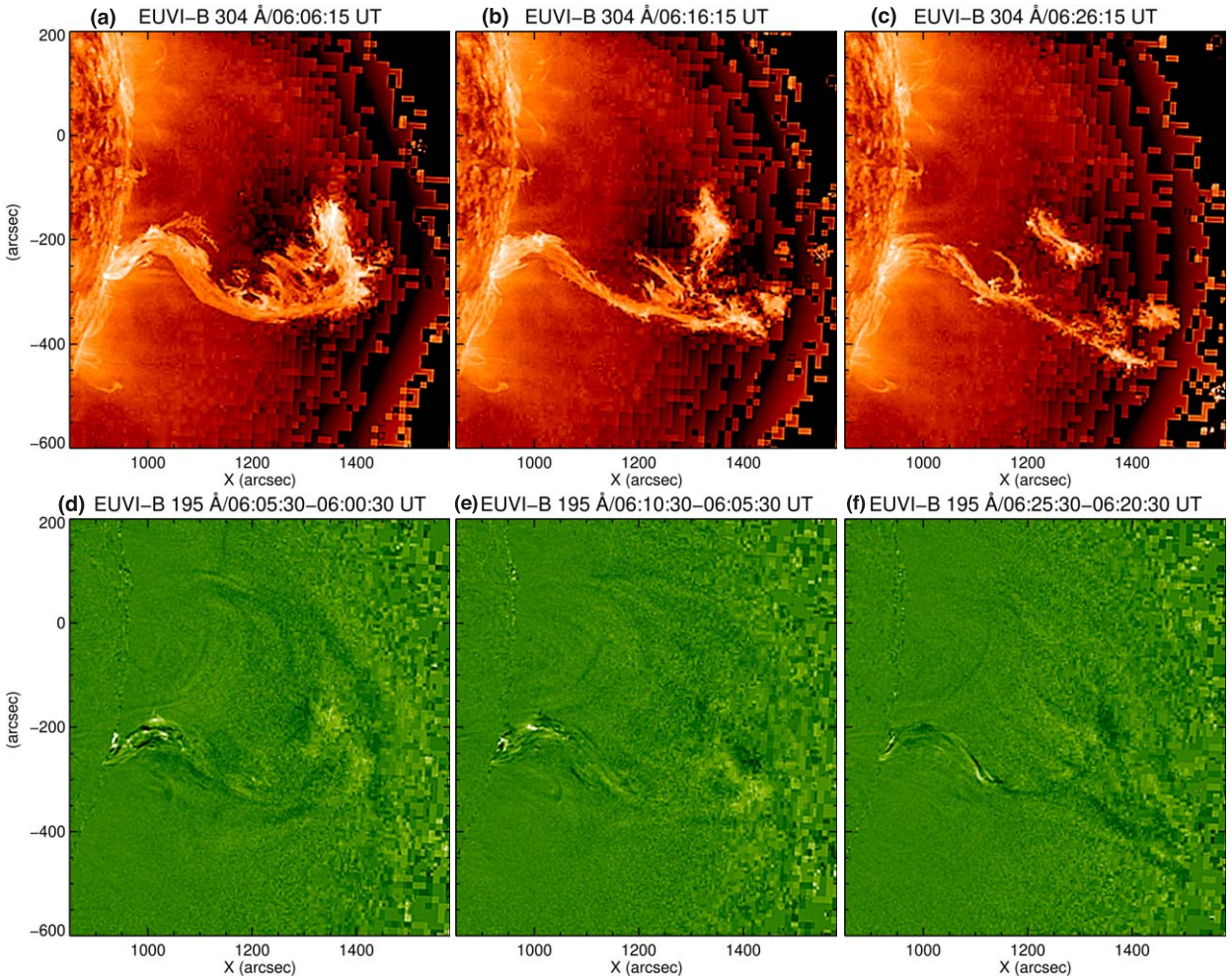


**Figure 8.** Sequence of STEREO-B EUVI 304 and 195 Å running-difference images showing the erupting prominence stalling and falling after it reached the pseudo-streamer. Note that the north leg is detached. An animation of panels (d)–(f) is available online, showing the STEREO-B EUVI 195 Å undifferenced images alongside the cotemporal running-difference images. The animation runs from 00:10:30 UT to 07:55:30 UT, and the duration is 7 s.

(An animation of this figure is available.)

fan, within the pseudo-streamer fan on the negative-polarity side (11,500 s). The red and yellow field lines highlight the conjugate footpoints of the reconnected flux rope at this time. Subsequently, as the inner flux system relaxes toward a nearly potential state, the twisted flux-rope field lines reconnect with other field lines inside the pseudo-streamer. This process produces multiple twisted structures that are disconnected from the embedded-bipole flux and reside within the larger-scale pseudo-streamer flux (12,500 s). These remnants of the filament-carrying flux rope end up as long, twisted flux tubes that lie above the inner null N1 and below the outer null N2 (see animation accompanying Figure 14).

## 5. Discussion

The activity sequence revealed by the simulation provides a clear interpretation of the observed evolution of this stalled eruption. Key features are marked accordingly in the AIA 171/131 Å images of Figure 16. During the interval between the B- and C-class flares, localized EUV and soft X-ray brightenings and flows indicate ongoing energy release, possibly due to component reconnection between the arch filaments in the northern section of the filament channel (Figure 4). The AR eruption proceeds exactly as expected from the breakout model: the free energy built up by footpoint motions is sufficient to enable the flux and embedded cool plasma in the filament channel to rise, exerting pressure on the inner null N1 and distorting it into a BCS. As the BCS elongates and bulges outward, inner-fan flux reconnects with adjacent pseudo-streamer flux, forming plasmoids that stream toward the edges of the sheet. A thin bright FCS forms beneath the rising flux, enabling reconnection in the filament channel to create a flux rope. A bright flare arcade forms and grows from 05:35 UT onward, joined to the rising flux rope by the lengthening FCS. The onset of flare reconnection is accompanied by a narrow row of remote brightenings south of the southern flux-rope footpoint, indicative of intense breakout reconnection as the flux rope penetrates into the pseudo-streamer.

A striking common feature is seen in the simulation and the observations: The northern flux-rope leg disconnects from its original location and reappears with its footpoint in the pseudo-streamer fan around 16,000 s and 05:54 UT, respectively. We attribute this change to extensive reconnection between the flux rope and the pseudo-streamer flux, which transfers much of the flux-rope twist onto pseudo-streamer field lines. This twisted

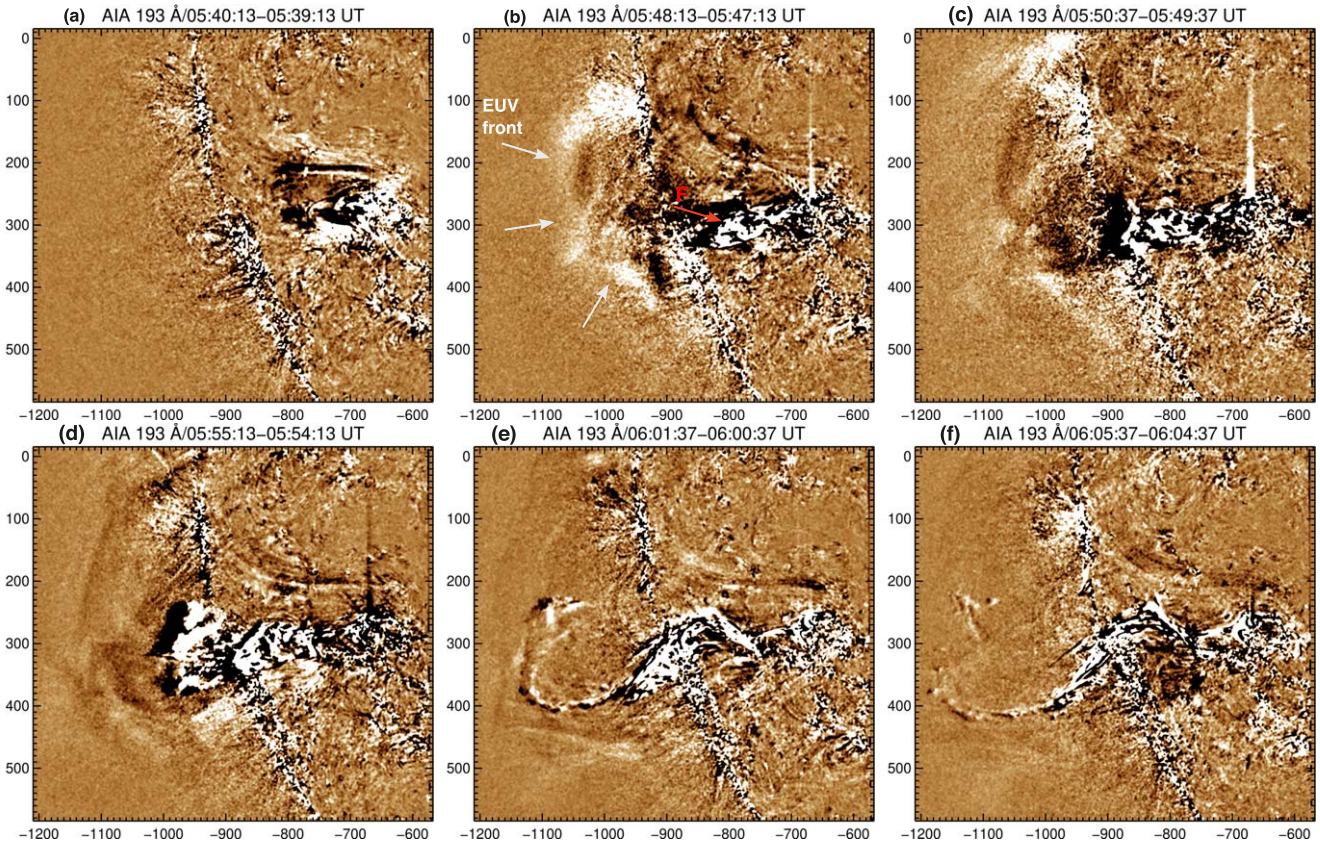


**Figure 9.** Selected AIA 193 Å running-difference images showing the ejected disturbances at and beyond the east limb. The EUV wave (marked by arrows) appears ahead of the plasma ejecta. F = filament. *X*- and *Y*-axes are labeled in arcseconds. An animation is available online. The animation runs from 05:02:49 UT to 06:57:25 UT, and the duration is 11 s.

(An animation of this figure is available.)

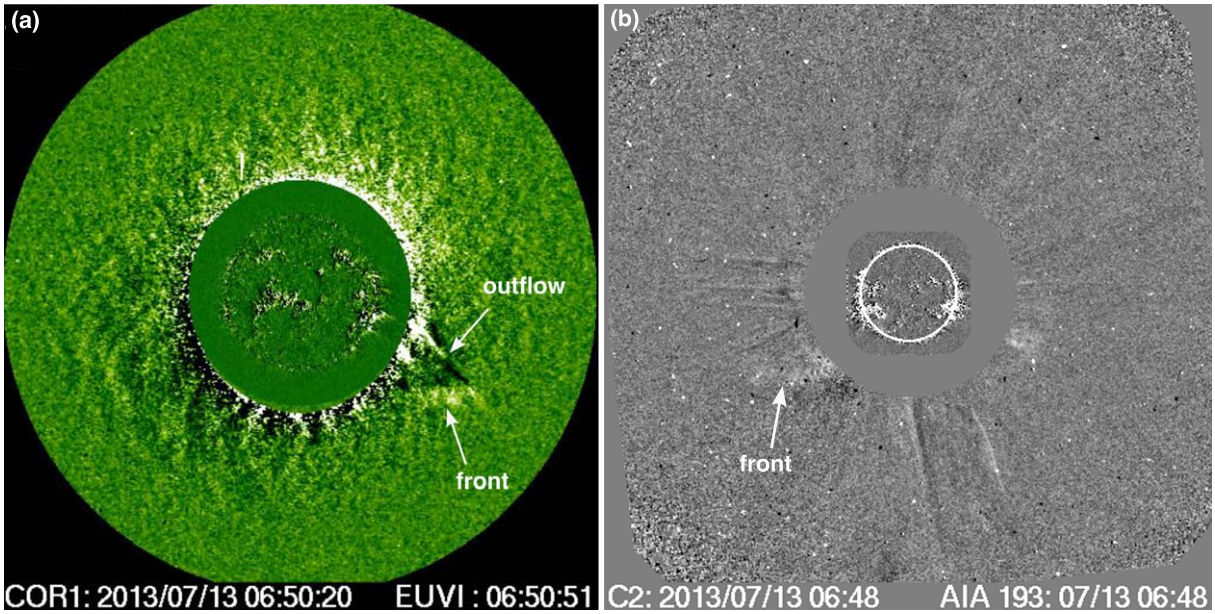


**Figure 10.** (a) Combined STEREO-B/EUVI 195 Å inner running-difference image and STEREO-B/COR1 outer running-difference image showing a faint front ahead and south of a thin linear feature. (b) Combined SDO/AIA 193 Å running-difference image of the solar disk and SOHO/LASCO C2 running-difference image showing a faint moving front off the southeast limb. The separation angle between SDO (and SOHO) and STEREO-B was 139° at this time.

bundle of field lines has metamorphosed significantly from the original filament flux rope, but it retains some coherent structure as the evolution proceeds. In the simulation, a substantial amount of twist distributed among multiple flux tubes remains confined within the pseudo-streamer after the jet is launched from the breakout sheet (see Figure 14). This yields

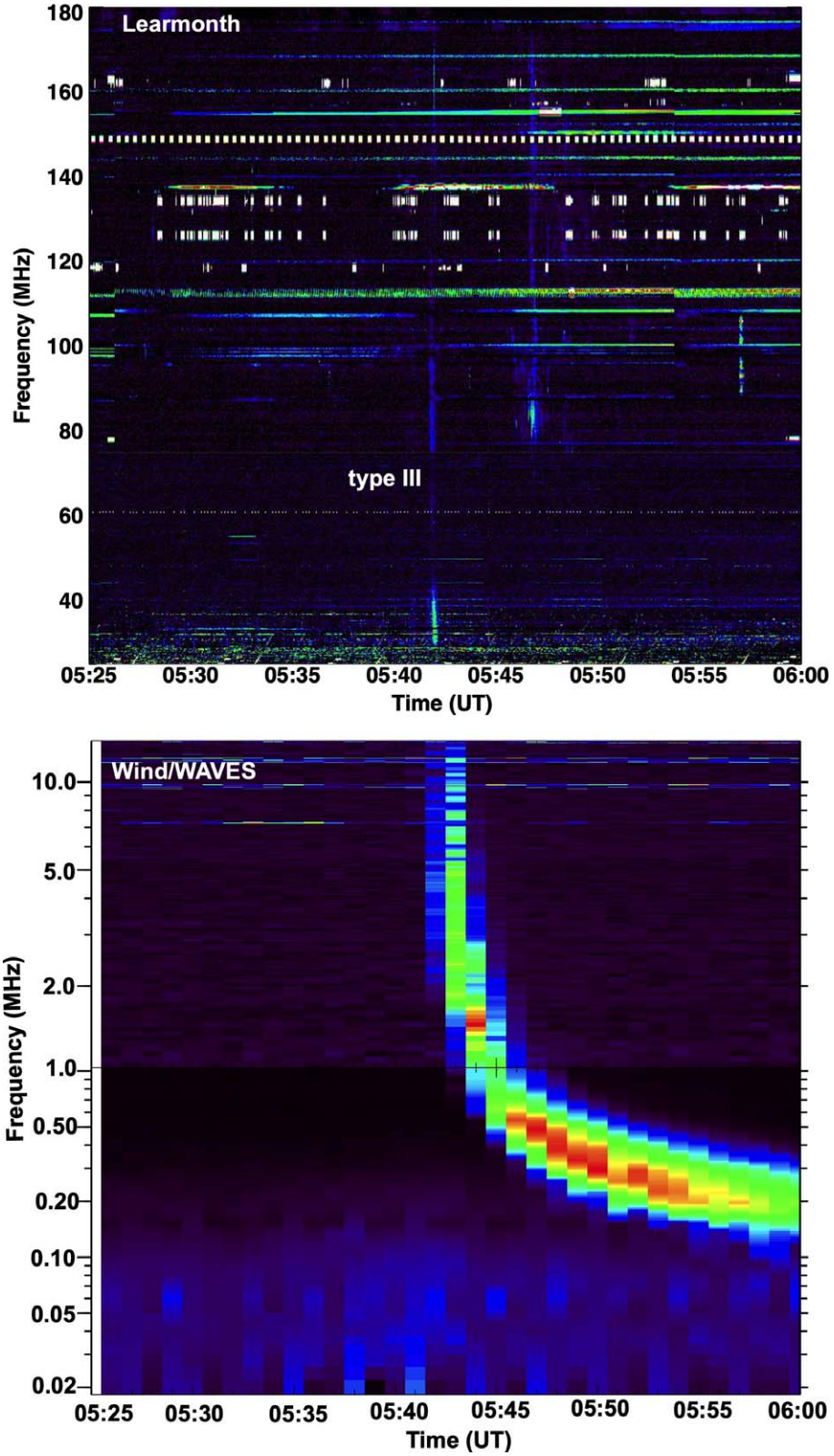


**Figure 11.** Radio spectra from Learmonth radio observatory (top, 25–180 MHz) and Wind/WAVES (bottom, 0.2–16 MHz) showing Type III bursts during the impulsive phase.

numerous filamentary currents surrounded by current sheaths separating reconnected twist flux from ambient untwisted flux, analogous to the reconnection-driven current filamentation phenomenon (Karpen et al. 1998). Note also that, since only a weak jet was evident in the simulation and the observations, most of the magnetic helicity associated with the filament channel must be retained in the system, presumably as small-scale twisting and tangling of the large-scale, closed

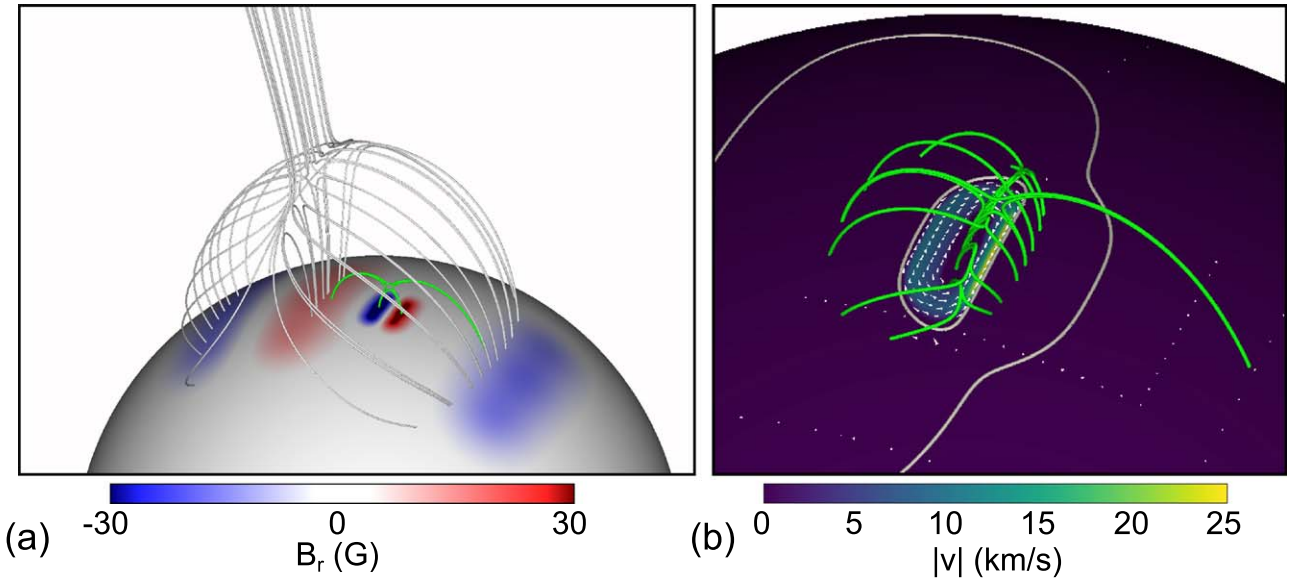


**Figure 12.** (a) Initial configuration of the three-dimensional MHD simulation. Gray field lines are rooted in the weak positive-polarity (red) and negative-polarity (blue) footpoints of the pseudo-streamer. Green field lines outline the separatrix in the midplane of the strong inner fan-spine system. (b) Flow field at the base of the inner fan-spine system; vectors are superposed on the magnitude (color shading). Green field lines outline the separatrix and spine of the inner embedded bipole. Gray solid lines on the surface mark the inner and outer PILs. See text for details.

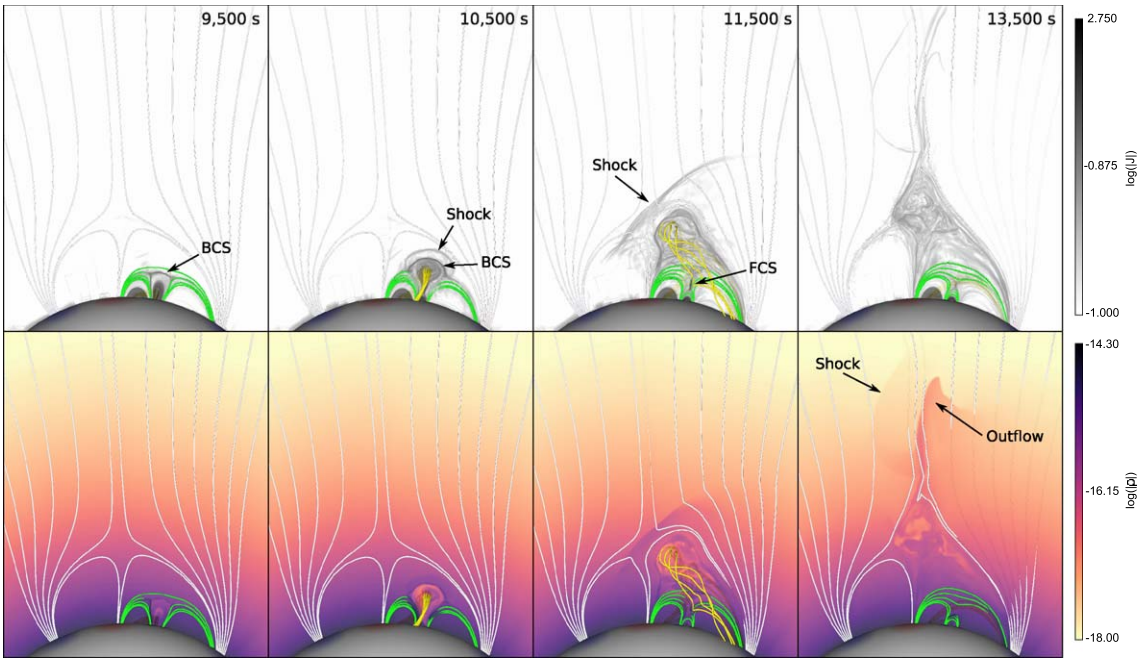


**Figure 13.** Side view of results at four times during the simulation. Top row: log(current density) (grayscale, where units of current are statampere per cubic centimeter) and field lines (gray are from the pseudo-streamer, yellow and green are from the inner fan-spine system). Bottom row: log(mass density) (color scale, where units of density are grams per cubic centimeter) and field lines (white are from the pseudo-streamer, green and yellow are from the inner fan-spine system).

pseudo-streamer flux. This is likely to be the case for all confined eruptions: The helicity associated with the localized filament-channel flux must end up as twists and tangles of the overlying background coronal field.

The remote ribbon appeared during the phase of explosive breakout reconnection when the rising flux rope reconnected with the surrounding pseudo-streamer flux. We detected multiple plasmoids at the top of the flux rope shortly before the appearance of the remote ribbon. The size of the plasmoids (2″–3″) is consistent with previous observations of plasmoids associated with breakout jets (Kumar et al. 2019a, 2019b). The first RHESSI X-ray source is interpreted as a looptop source (above the flare arcade) that appeared during flare reconnection in the FCS underneath the rising flux rope. RHESSI and AIA observations reveal that the second X-ray source which appeared at the top of the side arcade formed shortly after the onset of explosive breakout reconnection. Similar second X-ray looptop sources have been detected during flux-rope

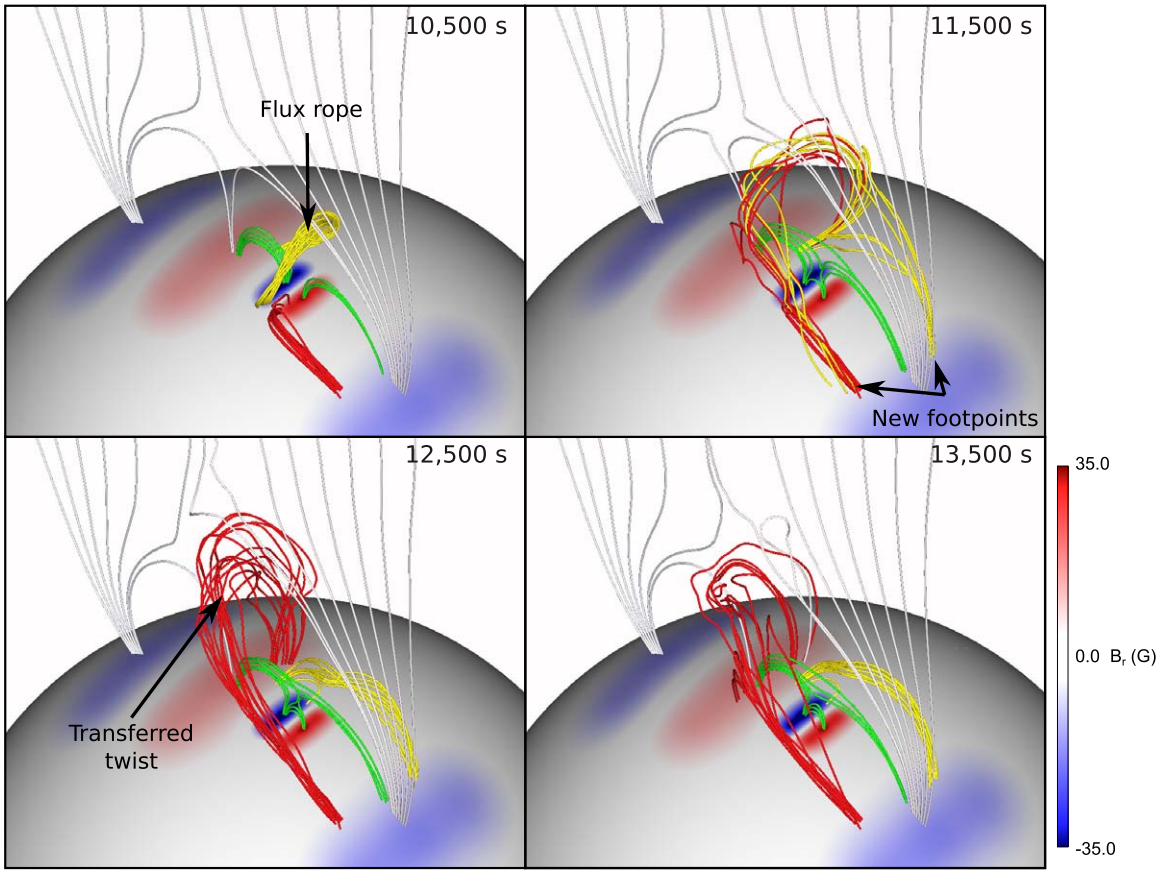


**Figure 14.** Oblique view of results at four times during the simulation. Red and blue patches on the surface mark positive- and negative-polarity surface flux densities, respectively. Gray field lines show the pseudo-streamer and are traced from footpoints rooted in the large-scale negative (blue) polarities. Green: the inner fan-spine system, with footpoints rooted in both positive (red) polarities. Red: footpoints rooted in the rightmost negative polarity. Yellow: footpoints rooted in the large-scale positive polarity. An animation is available showing the evolution. The duration is 7 s and runs from $t = 0$ to 20,500 s.

(An animation of this figure is available.)

eruptions in pseudo-streamers at the limb (Kumar et al. 2021). The simultaneous appearance of narrow Type IIIs during breakout reconnection suggests the escape of electron beams from the reconnection site at the top of the pseudo-streamer to interplanetary space.

As shown in Figures 5 and 8, the flux rope stalls, flattens, and disappears without leaving the pseudo-streamer. We observed similar behavior in a failed eruption that did not originate in a nested fan-spine system, but simply encountered strong overlying flux from a nearby AR (Kumar et al. 2022, 2023). Based on the simulation in Section 5, we conclude that the flux rope in that case was unable to drive much reconnection through the pseudo-streamer null point and BCS. In contrast, the existence of faint but distinct fronts visible in STEREO COR1 and LASCO C2 demonstrates that some mass and energy were transferred out of the pseudo-streamer in the nested-flux-system event. According to the simulation, the outer front is a shock generated by the explosive onset of the inner eruption, while the inner front is a weak jet propagating along the pseudo-streamer spine. The shock appears to convert from a parallel shock when exiting the inner fan to an oblique shock when exiting the pseudo-streamer.

Both the observations and the simulation demonstrate an initially fast eruption that stalls and "transforms" into a weak jet. The simulation shows a shock ahead of the flux rope, indicating that the eruption accelerated rapidly, and the observations show an intense flare, indicating that the energy release powering the eruption is explosive. This was clearly not a weak, slow eruption that simply ran out of steam; so why did the eruption stall, given that it started off so strongly? We propose that the double-breakout configuration naturally leads to rapid onset followed by stalling of an initially fast eruption.

Consider the generic scenario of three flux systems separated by two null points: a lower one that contains the erupting flux, a middle system that acts as a strapping field, and an upper system that also acts as a strapping field (which could be open or closed). In our particular case (Figure 13), the lower level corresponds to the closed AR field with a filament channel, the middle level to the overlying pseudo-streamer closed field, and the upper level to the external flux. As a result of the buildup of stress at the PIL of the inner flux system, the whole inner system expands, deforming both nulls into current sheets. The key point is that the field changes direction at each of these sheets, so the lower and upper fluxes are parallel while the middle flux is anti-parallel to the other two. Breakout reconnection at the two sheets erodes the middle-level strapping field from both directions, more efficiently than in the single-null case, leading to fast rise of the filament-channel field, the onset of flare reconnection, and the acceleration of the ensuing flux rope. When this flux rope impacts the null region in a single-null configuration, very fast reconnection with the external flux drives a strong jet (e.g., Karpen et al. 2017; Wyper et al. 2017). In our double-null case, however, the flux rope field is directed in the same sense as the external flux, so if the flux rope reaches the

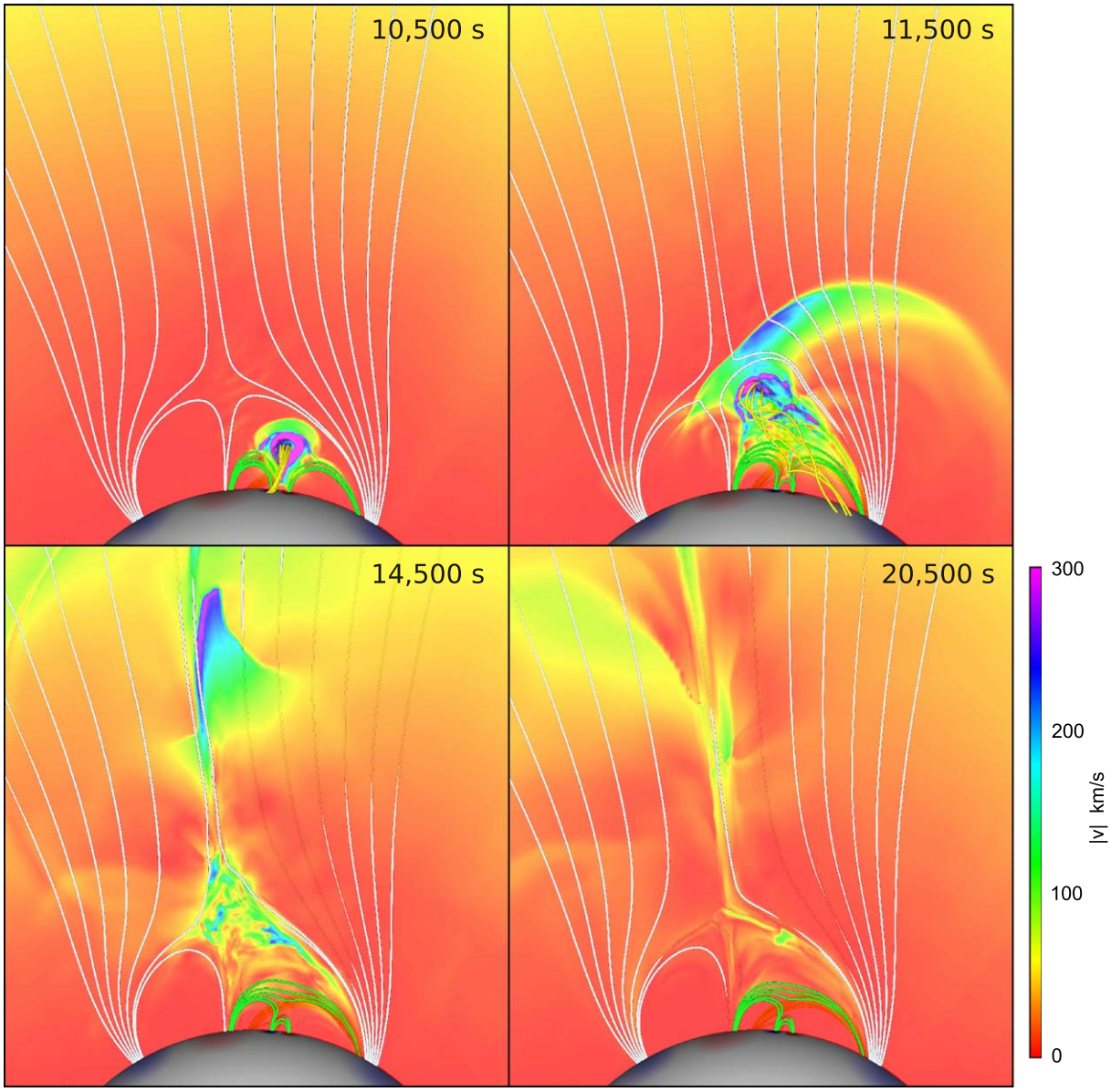


**Figure 15.** Side view of velocity magnitude in the midplane at four times during the simulation. The color bar shows the speed scale. The surface gray shading and field line colors are the same as in Figure 14. An animation is available showing the evolution. The duration is 7 s and runs from $t = 0$ to 20,000 s.

(An animation of this figure is available.)

outer null, it essentially hits a wall—exactly the behavior seen in Figure 13. Instead of reconnecting with the external field and escaping, the flux rope primarily disperses its twist and shear within the closed pseudo-streamer. Note that in three dimensions the flux rope could kink and rotate, so that reconnection with the open flux could become more favorable. Therefore, this simple model for failed eruptions must be tested with detailed calculations.

## 6. Conclusions

We have presented observations and simulations of an eruption that starts as a shock-associated flux-rope ejection but transforms into a weak jet. The underlying magnetic structure is atypical: an AR embedded in a large pseudo-streamer, giving rise to a pair of nested fan-spine topologies. The inner (AR) eruption drove a shock ahead of it, which manifested as an EUV wave, and was accompanied by a C1.4-class flare with a range of impulsive emissions, from hard X-rays to Type III bursts. Despite the energetic nature of this eruption, the flux rope became ensnared in the surrounding pseudo-streamer flux and underwent significant connectivity changes, culminating in a weak breakout jet from the overlying pseudo-streamer null.

This intriguing event demonstrates the importance of topology in determining whether and how an eruption will escape from the Sun. Unlike breakout eruptions in ARs under helmet streamers or in coronal holes, the nested null-point flux topology offers a different set of challenges to the flux rope as it exits the inner fan-spine system. In particular, the flux rope cannot easily reconnect with the flux overlying the outer null point, because that flux will tend to be oriented parallel to the flux-rope field. This double-breakout system is likely to lead to stalled eruptions where a coherent flux rope forms and accelerates quickly, but then stops and stays within the closed corona. We conclude that observing and modeling more

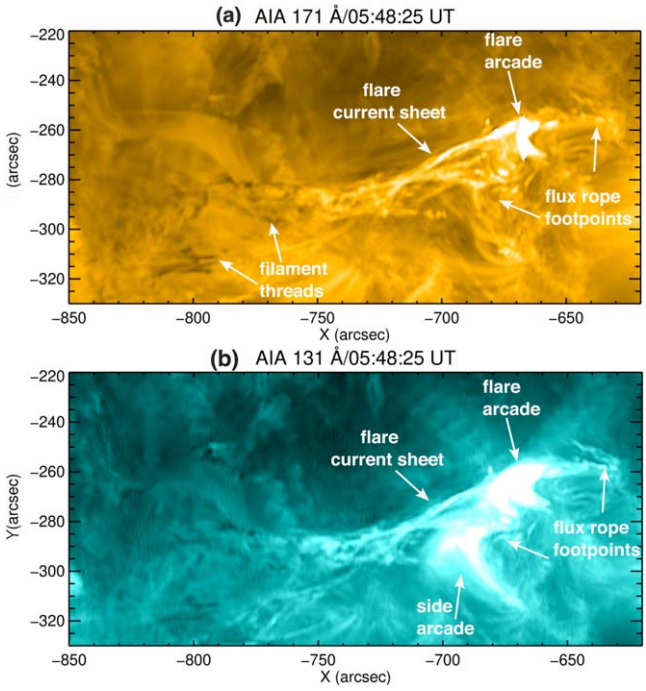


**Figure 16.** AIA 171 Å (a) and 131 Å (b) images at the same time during the impulsive phase. Key features are labeled based on the interpretation in the text. An animation of the AIA 131 Å images (panel (b)) is available online. The animation has two parts. The left side shows a larger region, with a smaller area outlined in red. The right side shows this smaller region. The animation runs from 05:01:37 UT to 06:56:25 UT, and the duration is 14 s.

(An animation of this figure is available.)

eruptions in nested magnetic flux systems may well solve the long-standing conundrum of why some eruptions generate CMEs, some generate jets, and others remain confined.

## Acknowledgments

SDO is a mission for NASA's Living With a Star (LWS) program. STEREO is a mission in NASA's Solar Terrestrial Probes program. This research was supported by NASA's Heliophysics Guest Investigator (grant No. 80NSSC20K0265), Supporting Research (grant No. 80NSSC24K0264), LWS Strategic Capability (grant No. 80NSSC22K0892), and GSFC Internal Scientist Funding Model (H-ISFM) programs, and by NSF Award Number 2229336. P.W. was supported by STFC (UK) consortium grant No. ST/W00108X/1. The computations were sponsored by allocations on Discover at NASA's Center for Climate Simulation and on the DiRAC Data Analytic system at the University of Cambridge, operated by the University of Cambridge High Performance Computing Service on behalf of the STFC DiRAC HPC Facility (www.dirac.ac.uk) and funded by BIS National E-infrastructure capital grant (ST/K001590/1), STFC capital grant Nos. ST/H008861/1 and ST/H00887X/1, and STFC DiRAC Operations grant No. ST/K00333X/1. DiRAC is part of the National E-Infrastructure.

## ORCID iDs

Judith T. Karpen https://orcid.org/0000-0002-6975-5642
Pankaj Kumar https://orcid.org/0000-0001-6289-7341
Peter F. Wyper https://orcid.org/0000-0002-6442-7818
C. Richard DeVore https://orcid.org/0000-0002-4668-591X
Spiro K. Antiochos https://orcid.org/0000-0003-0176-4312

## References

Antiochos, S. K. 1998, ApJL, 502, L181
Antiochos, S. K., DeVore, C. R., & Klimchuk, J. A. 1999, ApJ, 510, 485
Aschwanden, M. J., Metcalf, T. R., Krucker, S., et al. 2004, SoPh, 219, 149
Bougeret, J. L., Kaiser, M. L., Kellogg, P. J., et al. 1995, SSRv, 71, 231
Brueckner, G. E., Howard, R. A., Koomen, M. J., et al. 1995, SoPh, 162, 357
Cui, Y., Wang, H., Xu, Y., & Liu, S. 2018, JGRA, 123, 1704
Dahlin, J. T., Antiochos, S. K., & DeVore, C. R. 2019, ApJ, 879, 96
DeForest, C. E. 2017, ApJ, 838, 155
DeRosa, M. L., & Barnes, G. 2018, ApJ, 861, 131
DeVore, C. R., & Antiochos, S. K. 2008, ApJ, 680, 740
Duan, A., Jiang, C., & Feng, X. 2023, ApJ, 945, 102
Howard, R. A., Moses, J. D., Vourlidas, A., et al. 2008, SSRv, 136, 67
Karpen, J. T., Antiochos, S. K., DeVore, C. R., & Golub, L. 1998, ApJ, 495, 491
Karpen, J. T., Antiochos, S. K., & DeVore, C. R. 2012, ApJ, 760, 81
Karpen, J. T., DeVore, C. R., Antiochos, S. K., & Pariat, E. 2017, ApJ, 834, 62
Kazachenko, M. D. 2023, ApJ, 958, 104
Kumar, P., Karpen, J. T., Antiochos, S. K., Wyper, P. F., & DeVore, C. R. 2019a, ApJL, 885, L15
Kumar, P., Karpen, J. T., Antiochos, S. K., et al. 2019b, ApJ, 873, 93
Kumar, P., Karpen, J. T., Antiochos, S. K., et al. 2021, ApJ, 907, 41
Kumar, P., Karpen, J. T., Antiochos, S. K., et al. 2023, ApJ, 943, 156
Kumar, P., Nakariakov, V. M., Karpen, J. T., DeVore, C. R., & Cho, K.-S. 2022, ApJL, 932, L9
Kumar, P., Srivastava, A. K., Filippov, B., Erdélyi, R., & Uddin, W. 2011, SoPh, 272, 301
Lemen, J. R., Title, A. M., Akin, D. J., et al. 2012, SoPh, 275, 17
Li, T., Sun, X., Hou, Y., et al. 2022, ApJL, 926, L14
Lin, R., Dennis, B., Hurford, G., et al. 2002, SoPh, 210, 3
Lynch, B. J., Airapetian, V. S., DeVore, C. R., et al. 2019, ApJ, 880, 97
Lynch, B. J., Antiochos, S. K., DeVore, C. R., Luhmann, J. G., & Zurbuchen, T. H. 2008, ApJ, 683, 1192
Lynch, B. J., Masson, S., Li, Y., et al. 2016, JGRA, 121, 10677
Lynch, B. J., Palmerio, E., DeVore, C. R., et al. 2021, ApJ, 914, 39
MacNeice, P., Antiochos, S. K., Phillips, A., et al. 2004, ApJ, 614, 1028
Mason, E. I., Antiochos, S. K., & Vourlidas, A. 2021, ApJL, 914, L8
Masson, S., Antiochos, S. K., & DeVore, C. R. 2013, ApJ, 771, 82
Masson, S., Antiochos, S. K., & DeVore, C. R. 2019, ApJ, 884, 143
Metcalf, T. R., Hudson, H. S., Kosugi, T., Puetter, R. C., & Pina, R. K. 1996, ApJ, 466, 585
Müller, D., Nicula, B., Felix, S., et al. 2017, A&A, 606, A10
Pariat, E., Antiochos, S. K., & DeVore, C. R. 2009, ApJ, 691, 61
Pariat, E., Antiochos, S. K., & DeVore, C. R. 2010, ApJ, 714, 1762
Pariat, E., Dalmasse, K., DeVore, C. R., Antiochos, S. K., & Karpen, J. T. 2015, A&A, 573, A130
Pariat, E., Dalmasse, K., DeVore, C. R., Antiochos, S. K., & Karpen, J. T. 2016, A&A, 596, A36
Shen, Y., Liu, Y., & Su, J. 2012, ApJ, 750, 12
Shibata, K., Nitta, N., Strong, K. T., et al. 1994, ApJL, 431, L51
Svestka, Z., & Cliver, E. W. 1992, in IAU Coll. 133, Eruptive Solar Flares, ed. Z. Svestka, B. V. Jackson, & M. E. Machado (New York: Springer), 1
Thompson, W. T., Davila, J. M., Fisher, R. R., et al. 2003, Proc. SPIE, 4853, 1
Wang, Y. M., Sheeley, N. R., & Rich, N. B, J. 2007, ApJ, 658, 1340
Wuelser, J.-P., Lemen, J. R., Tarbell, T. D., et al. 2004, Proc. SPIE, 5171, 111
Wyper, P. F., Antiochos, S. K., & DeVore, C. R. 2017, Natur, 544, 452
Wyper, P. F., Antiochos, S. K., DeVore, C. R., et al. 2021, ApJ, 909, 54
Wyper, P. F., & DeVore, C. R. 2016, ApJ, 820, 77
Wyper, P. F., DeVore, C. R., & Antiochos, S. K. 2018a, ApJ, 852, 98
Wyper, P. F., DeVore, C. R., & Antiochos, S. K. 2019, MNRAS, 490, 3679
Wyper, P. F., DeVore, C. R., Antiochos, S. K., et al. 2022, ApJL, 941, L29
Wyper, P. F., DeVore, C. R., Karpen, J. T., & Lynch, B. J. 2016, ApJ, 827, 4
Wyper, P. F., DeVore, C. R., Karpen, J. T., Antiochos, S. K., & Yeates, A. R. 2018b, ApJ, 864, 165